

Augmenting Channel Charting with Classical Wireless Source Localization Techniques

Florian Euchner^{id}, Phillip Stephan^{id}, Stephan ten Brink^{id}

Institute of Telecommunications, Pfaffenwaldring 47, University of Stuttgart, 70569 Stuttgart, Germany
{euchner,stephan,tenbrink}@inue.uni-stuttgart.de

Abstract—Channel Charting aims to construct a map of the radio environment by leveraging similarity relationships found in high-dimensional channel state information. Although resulting channel charts usually accurately represent local neighborhood relationships, even under conditions with strong multipath propagation, they often fall short in capturing global geometric features. On the other hand, classical model-based localization methods, such as triangulation and multilateration, can easily localize signal sources in the global coordinate frame. However, these methods rely heavily on the assumption of line-of-sight channels and distributed antenna deployments. Based on measured data, we compare classical source localization techniques to channel charts with respect to localization performance. We suggest and evaluate methods to enhance Channel Charting with model-based localization approaches: One approach involves using information derived from classical localization methods to map channel chart locations to physical positions after conventional training of the forward charting function. Foremost, though, we suggest to incorporate information from model-based approaches during the training of the forward charting function in what we call “augmented Channel Charting”. We demonstrate that Channel Charting can outperform classical localization methods on the considered dataset.

Index Terms—Channel Charting, massive MIMO, localization

I. INTRODUCTION

Wireless localization systems are commonplace: Smartphones and cars navigate thanks to global navigation satellite systems (GNSSs), lost items can be found with the help of ultra-wideband (UWB) tags, Bluetooth beacons enable localization of assets in factories and emergency responders can access approximate caller locations determined by the cellular network. Many common wireless localization systems rely on a few common of techniques to determine the position of user equipments (UEs) (like smartphones, beacons or cars), namely angle of arrival (AoA) estimation and subsequent triangulation, time of arrival (ToA) estimation and subsequent multilateration, receive power-based multilateration or a combination of aforementioned methods. What these localization techniques have in common is that they are *model-based*: They rely on the assumption of a certain channel model, for example relying on the existence of a sufficiently strong line-of-sight (LoS) channel, or assuming a certain fading model with a specific path loss coefficient.

This work is supported by the German Federal Ministry of Education and Research (BMBF) within the projects Open6GHub (grant no. 16KISK019) and KOMSENS-6G (grant no. 16KISK113).

More recently, the concept of Channel Charting has been introduced [1] as a data-driven approach that learns a so-called channel chart, a kind of map of the radio environment. One of the initially proposed applications of Channel Charting was *relative* localization, but additional work suggested various methods to also enable localization in the absolute global coordinate frame [2] [3]. In contrast to model-based techniques, Channel Charting relies on similarity relationships between measured channel state information (CSI) and thereby specifically exploits the multipath characteristics of the propagation environment.

So far, Channel Charting and model-based localization have only been considered separately, but were never compared to each other or even combined. In this work, we address this gap by directly comparing and combining model-based approaches and Channel Charting. All evaluations are performed on one particular dataset of CSI measurements that is introduced in Section II. In Section III, we explain the classical model-based localization methods and evaluate their performance, and in Section IV, we evaluate the performance of Channel Charting-based localization. Subsequently, in Section V, we combine classical techniques with Channel Charting into what we call *augmented* Channel Charting, and finally, in Section VI, we compare the performance of all methods with respect to various metrics. The datasets and source code for both classical and Channel Charting-based localization used by this work are publicly available¹.

II. DATASET AND SYSTEM MODEL

As in our previous work on Channel Charting [4], we learn the channel chart for a dataset generated by *Distributed Channel Sounder by University of Stuttgart (DICHASUS)*, our distributed massive multiple-input multiple-output (mMIMO) channel sounder, whose architecture is thoroughly described in [5]. In brief, DICHASUS measures the propagation channel between a single transmitter and many receive antennas. It achieves long-term phase-coherence, even if antennas are distributed over a wide area. DICHASUS provides large datasets containing frequency-domain CSI tensors $\mathbf{H}^{(l)}$, alongside side information like timestamps and accurate information about the positions of all antennas.

The dataset chosen for the following analyses is called *dichasus-cf0x* [6], and was captured in an industrial environ-

¹<https://github.com/Jeija/ToA-AoA-Augmented-ChannelCharting/>

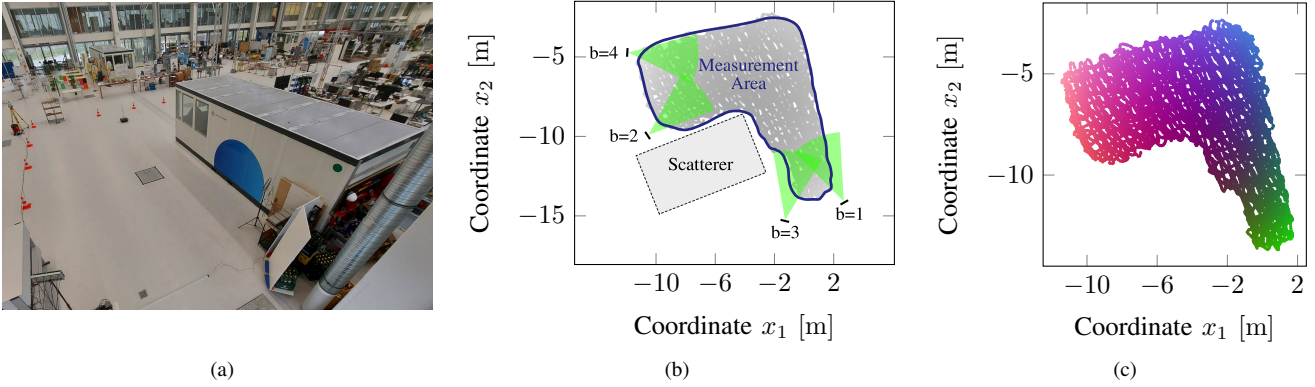


Fig. 1. Information about the environment the dataset was measured in: The figure shows (a) a photograph of the environment, (b) a top view map and (c) a scatter plot of colored “ground truth” positions of datapoints in $\mathcal{S}_{\text{full}}$, colored with the measured delay spread. The antenna arrays in the map are drawn to scale as black rectangles and their viewing direction is indicated by the green sectors.

ment with $B = 4$ separate uniform planar arrays (UPAs) with half-wavelength antenna spacing, made up of $M_{\text{row}} \times M_{\text{col}} = 2 \times 4$ antennas each. $N_{\text{sub}} = 1024$ orthogonal frequency division multiplex (OFDM) channel coefficients were measured at a carrier frequency of 1.272 GHz and with a total bandwidth of 50 MHz. The complex-valued channel coefficients of all arrays, antennas and subcarriers for time instance l are stored in the tensor $\mathbf{H}^{(l)} \in \mathbb{C}^{B \times M_{\text{row}} \times M_{\text{col}} \times N_{\text{sub}}}$. For example, $H_{2,1,3,400}$ is the subcarrier coefficient of the 400th subcarrier of the third antenna in the first row of antenna array $b = 2$.

The single dipole transmit antenna is mounted on top of a robot, which travels along a set of trajectories inside a defined, L-shaped area, with an overall bounding box size of approximately 14 m \times 14 m. A prism is attached to the tip of the antenna and tracked with millimeter-level precision by a tachymeter, providing “ground truth” positions $\mathbf{x}^{(l)}$. In addition to CSI and reference positions, timestamps $t^{(l)}$ are recorded. Thus, the complete dataset can be represented as the following set containing a total of L datapoints:

$$\text{Dataset} : \mathcal{S} = \left\{ \left(\mathbf{H}^{(l)}, \mathbf{x}^{(l)}, t^{(l)} \right) \right\}_{l=1, \dots, L}$$

A photo and a top view map of the environment are shown in Fig. 1. A large metal container is located at the inner corner of the L-shape, blocking the LoS. The true datapoint positions $\mathbf{x}^{(l)}$ are shown in Fig. 1. The points have been colorized and the datapoints will retain their color even as the FCF maps them to a position in the channel chart. This allows for a visual evaluation of the generated chart: If the global topology is preserved, a similar color gradient should appear in the chart. If the local geometry is preserved, only datapoints with similar colors should be close to each other in the channel chart.

Thanks to synchronization and the distributed setup of the antenna arrays, time of arrival-based multilateration should be possible in principle (though limited in accuracy by the bandwidth of the system). Also, since there are $M_{\text{row}} = 4$ antennas in one row of an antenna array, the azimuth angle of arrival can be estimated and triangulation should be possible.

The centers of the $B = 4$ antenna arrays are known to be at $\mathbf{z}^{(b)} \in \mathbb{R}^3$, and the antenna normal vectors are $\mathbf{n}^{(b)} \in \mathbb{R}^3$.

In all localization tasks, we assume that the height of the transmitter is known and constant, i.e., we provide $x_3^{(l)}$ to the estimation algorithm. This simplifies the estimation task to two-dimensional localization. This assumption of a constant transmitter height is approximately true, because the robot always remains on the factory floor and that floor is almost perfectly flat.

III. CLASSICAL LOCALIZATION TECHNIQUES

A. Time of Arrival Estimation and Multilateration

The two steps involved in ToA-based multilateration are to first estimate the ToAs for all antenna arrays and to then use that information to determine the transmitter location. Various approaches and algorithms have been proposed for each of these steps. In our case, we use a root-Multiple Signal Classification (MUSIC) super-resolution algorithm for ToA estimation, and a maximum likelihood (ML)-based approach for the second step.

1) *Time of Arrival Estimation:* Even though, in theory, every single antenna has its own ToA, we assume that the times of arrival within one antenna array are similar enough due to the small antenna spacing and just compute one delay per antenna array. We proceed as described in [7]: To reduce the computational load, we do not compute the subcarrier autocorrelation matrix \mathbf{R} over all $N_{\text{sub}} = 1024$ subcarriers, but split the subcarriers into $U = 4$ segments of length $V = 256$, such that the modified CSI tensor for one datapoint can be written as $\tilde{\mathbf{H}}^{(l)} \in \mathbb{C}^{B \times M_{\text{row}} \times M_{\text{col}} \times U \times V}$. The autocorrelation matrix $\mathbf{R}^{(l,b)} \in \mathbb{C}^{V \times V}$ for antenna array b and time index l is then estimated as

$$\hat{\mathbf{R}}^{(l,b)} = \frac{1}{M_{\text{row}} \cdot M_{\text{col}} \cdot U} \sum_{m_r=1}^{M_{\text{row}}} \sum_{m_c=1}^{M_{\text{col}}} \sum_{u=1}^U \tilde{\mathbf{H}}_{b,m_r,m_c,u}^{(l)} \left(\tilde{\mathbf{H}}_{b,m_r,m_c,u}^{(l)} \right)^H,$$

where $\tilde{\mathbf{H}}_{b,m_r,m_c,u}^{(l)} \in \mathbb{C}^V$. We found that the accuracy of ToA estimates improves when applying the forward-backward

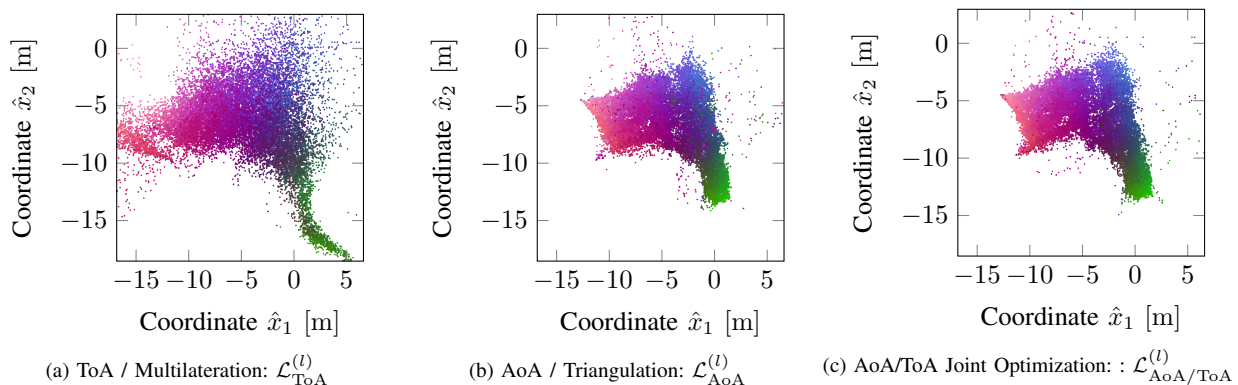


Fig. 2. Position estimates for the considered classical source localization techniques

correlation matrix (FBCM) method as mentioned in [7]. We therefore compute the FBCM corresponding to $\hat{\mathbf{R}}^{(l,b)}$ as

$$\hat{\mathbf{R}}_{\text{FBCM}}^{(l,b)} = \frac{1}{2} \left(\hat{\mathbf{R}}^{(l,b)} + \mathbf{J} \left(\hat{\mathbf{R}}^{(l,b)} \right)^* \mathbf{J} \right),$$

where $(\cdot)^*$ symbolizes the complex conjugate, and \mathbf{J} is the $V \times V$ exchange matrix, where all entries are equal to zero except for those on the anti-diagonal, which are equal to one. We determine the number of sources (i.e., number of multipath components), which is a required input for MUSIC, using a Rissanen minimum descriptive length (MDL) criterion as in [8]. We then proceed to find the powers and ToAs of all sources from $\hat{\mathbf{R}}_{\text{FBCM}}^{(l,b)}$ using the root-MUSIC algorithm. Out of a subset of a few strongest sources (highest receive powers), we pick the earliest one, assuming that it corresponds to the LoS propagation path, if one exists, or to the shortest propagation path otherwise.

The result of the procedure are ToA estimates $\hat{\tau}^{(l,b)}$, with $B = 4$ estimates (one for each antenna array) for every time instance l . It is important to stress that while the ToAs can be estimated, the time of transmission (ToT) $\tau_{\text{TX}}^{(l)}$ is unknown, as receivers and transmitter are not synchronized.

2) *Maximum Likelihood Multilateration*: Now that ToA estimates $\hat{\tau}^{(l,b)}$ are available, we can define a function that determines the likelihood that the transmitter is located at any particular position $\mathbf{x} \in \mathbb{R}^3$. As an abbreviation, we introduce

$$d^{(b)}(\mathbf{x}) = \left\| \mathbf{x} - \mathbf{z}^{(b)} \right\|_2,$$

which is the Euclidean distance between the transmitter location \mathbf{x} and antenna array b located at $\mathbf{z}^{(b)}$, and let c_0 denote the speed of light. These are two ways to deal with the unknown ToT $\tau_{\text{TX}}^{(l)}$:

a) *Treat $\tau_{\text{TX}}^{(l)}$ as a nuisance parameter*: Inspired by [9], we model the ToA estimation error as a normally distributed random variable and derive the likelihood function as

$$\begin{aligned} & \mathcal{L}_{\text{ToA}}^{(l)}(\mathbf{x}, \tau_{\text{TX}}) \\ &= \prod_{b=1}^B \frac{1}{\sqrt{2\pi}\sigma^{(l,b)}} \cdot \exp \left(-\frac{1}{2} \left(\frac{d^{(b)}(\mathbf{x}) - \hat{\tau}^{(l,b)} + \tau_{\text{TX}}}{\sigma^{(l,b)}} \right)^2 \right). \end{aligned} \quad (1)$$

Eq. (1) computes the likelihood that the transmitter is located at $\mathbf{x} \in \mathbb{R}^3$ for an assumed ToT of τ_{TX} . The variance parameter $\sigma^{(l,b)}$ is determined based on a heuristic that takes into account the observed root mean square (RMS) delay spread at array b for datapoint l .

b) *Rely on time differences*: Absolute ToAs $\hat{\tau}^{(l,b)} - \tau_{\text{TX}}^{(l)}$ are influenced by the ToT. However, the difference in ToA, usually referred to as the time difference of arrival (TDoA), between arrays, is independent of the ToT. Again under the assumption of a normally distributed ToA estimation error, we define a TDoA-based likelihood function

$$\begin{aligned} \mathcal{L}_{\text{TDoA}}^{(l)}(\mathbf{x}) &= \prod_{b_1=1}^{B-1} \prod_{b_2=b_1+1}^B \frac{1}{\sqrt{2\pi}\sigma^{(l,b_1,b_2)}} \\ &\cdot \exp \left(-\frac{1}{2} \left(\frac{\frac{d^{(b_2)}(\mathbf{x}) - d^{(b_1)}(\mathbf{x})}{c_0} - (\hat{\tau}^{(l,b_2)} - \hat{\tau}^{(l,b_1)})}{\sigma^{(l,b_1,b_2)}} \right)^2 \right) \end{aligned} \quad (2)$$

where $\sigma^{(l,b_1,b_2)}$ in Eq. (2) is again determined using a heuristic based on the observed RMS delay spread of arrays b_1 and b_2 for datapoint l .

After defining $\mathcal{L}_{\text{ToA}}^{(l)}$ and $\mathcal{L}_{\text{TDoA}}^{(l)}$, we estimate the transmitter location by performing ML estimation. We found that optimizing $\mathcal{L}_{\text{ToA}}^{(l)}$ over both \mathbf{x} and τ_{TX} provides better performance than optimizing $\mathcal{L}_{\text{TDoA}}^{(l)}$ over \mathbf{x} :

$$\left(\hat{\mathbf{x}}^{(l)}, \hat{\tau}_{\text{TX}}^{(l)} \right) = \arg \max_{(\mathbf{x}, \tau_{\text{TX}})} \mathcal{L}_{\text{ToA}}^{(l)}(\mathbf{x}, \tau_{\text{TX}})$$

We use SciPy's implementation of the Broyden-Fletcher-Goldfarb-Shanno (BFGS) algorithm for ML optimization. The TDoA-based likelihood function $\mathcal{L}_{\text{TDoA}}^{(l)}$ proved useful for initialization: We initialize the BFGS algorithm with a position determined in a previous step by evaluating $\mathcal{L}_{\text{TDoA}}^{(l)}$ on a grid of candidate positions \mathbf{x} and picking the most likely result. A more computationally efficient procedure is described in [9].

3) *Results*: The colored location estimates $\hat{\mathbf{x}}^{(l)}$ obtained through multilateration are shown in Fig. 2a. Some overall features of the environment are preserved, but the L-shape is heavily distorted and the estimates appear to be very noisy. Refer to Section VI for performance metrics and a comparison to the other source localization techniques.

B. Angle of Arrival Estimation and Triangulation

Triangulation determines the transmitter position using the AoAs of the received LoS components at all antenna arrays (assuming a LoS channel even exists). In the following, we first extract the LoS component from the channel tensor $\mathbf{H}^{(l)}$, we then estimate all AoAs using MUSIC and finally determine the transmitter location, again using ML optimization. We restrict ourselves to using the azimuth AoA, as the elevation AoA estimate would not be very accurate (only two rows in the antenna arrays) and also would not contribute much due to the overall geometry of the setup.

1) *Line of Sight Component Extraction*: We found that the ToA estimates derived for multilateration may be used to also improve AoA estimation. Since estimated ToAs $\hat{\tau}^{(l,b)}$ should ideally indicate the time of arrival of the LoS component, we can use them to isolate said component from all the other multipath components in the channel impulse response (CIR):

$$H_{b,m_r,m_c}^{(l)} = \sum_{n=1}^{N_{\text{sub}}} \exp\left(j2\pi\hat{\tau}^{(l,b)}\frac{n - N_{\text{sub}}/2 - 1}{N_{\text{sub}}}\right) H_{b,m_r,m_c,n}^{(l)} \quad (3)$$

In essence, Eq. (3) is derived from the inverse Fourier transform and evaluates the reconstructed continuous-time CIR at time $\hat{\tau}^{(l,b)}$. The results are collected in vectors $\mathbf{H}_{b,m_r}^{(l)} \in \mathbb{C}^{M_{\text{row}}}$, which contain the LoS component channel coefficient (if a LoS exists) for all antennas in row m_r .

2) *Angle of Arrival Estimation*: Next, for each datapoint l and antenna array b , the array correlation matrix $\mathbf{A}^{(l,b)}$ is estimated over all rows of the UPA. That is, $\mathbf{A}^{(l,b)}$ may be used to estimate the azimuth AoA, but contains no information about the elevation AoA:

$$\hat{\mathbf{A}}^{(l,b)} = \sum_{m_r=1}^{M_r} \mathbf{H}_{b,m_r}^{(l)} \left(\mathbf{H}_{b,m_r}^{(l)}\right)^H \in \mathbb{C}^{M_c \times M_c}$$

Under the assumption of a single source, we apply the root-MUSIC algorithm to $\hat{\mathbf{A}}^{(l,b)}$ (without FBCM computation) to find azimuth AoA estimates $\hat{\alpha}^{(l,b)}$ from $\hat{\mathbf{A}}^{(l,b)}$ for each datapoint and each antenna array. An azimuth AoA of $\hat{\alpha}^{(l,b)} = 0^\circ$ indicates that the signal arrives directly from the front.

3) *Maximum Likelihood Trilateration*: We derive an AoA-based likelihood function under the assumption that angle estimation errors are *von Mises*-distributed. We denote by $\angle_{\text{az}}(\mathbf{x} - \mathbf{z}^{(b)}, \mathbf{n}^{(b)})$ the azimuth angle between $\mathbf{x} - \mathbf{z}^{(b)}$ (the transmitter position relative to antenna array b) and $\mathbf{n}^{(b)}$ (the normal vector of antenna array b), i.e., the ideal AoA that corresponds to transmitter position \mathbf{x} for antenna array b . With I_0 denoting the modified Bessel function of the first kind of order 0, the AoA likelihood function is

$$\mathcal{L}_{\text{AoA}}^{(l)}(\mathbf{x}) = \prod_{b=1}^B \frac{\exp(\kappa^{(l,b)} \cos(\angle_{\text{az}}(\mathbf{x} - \mathbf{z}^{(b)}, \mathbf{n}^{(b)}) - \hat{\alpha}^{(l,b)}))}{2\pi I_0(\kappa^{(l,b)})}, \quad (4)$$

where $\kappa^{(l,b)}$ is a concentration parameter, which is also heuristically derived from the observed delay spread at array b for

datapoint l . As before, the transmitter position estimate is obtained by ML optimization using the BFGS algorithm:

$$\hat{\mathbf{x}}^{(l)} = \arg \max_{\mathbf{x}} \mathcal{L}_{\text{AoA}}^{(l)}(\mathbf{x})$$

4) *Results*: The colorized location estimates $\hat{\mathbf{x}}^{(l)}$ obtained through triangulation are shown in Fig. 2b. The L-shaped measurement environment is clearly visible, but the position estimate is clearly wrong for some datapoints, which appear as outliers. Refer to Section VI for performance metrics and a comparison to the other source localization techniques.

C. Joint Multilateration and Triangulation

The ML approach to position estimation can easily take into account information from multiple likelihood functions.

1) *Joint Likelihood*: We define joint likelihood functions

$$\begin{aligned} \mathcal{L}_{\text{AoA/TDoA}}^{(l)}(\mathbf{x}) &= \mathcal{L}_{\text{AoA}}^{(l)}(\mathbf{x}) \cdot \mathcal{L}_{\text{TDoA}}^{(l)}(\mathbf{x}) \text{ and} \\ \mathcal{L}_{\text{AoA/ToA}}^{(l)}(\mathbf{x}, \tau_{\text{TX}}) &= \mathcal{L}_{\text{AoA}}^{(l)}(\mathbf{x}) \cdot \mathcal{L}_{\text{ToA}}^{(l)}(\mathbf{x}, \tau_{\text{TX}}), \end{aligned}$$

which take into account both ToA and AoA estimates.

2) *Joint Maximum Likelihood Optimization*: We evaluate $\mathcal{L}_{\text{AoA/TDoA}}^{(l)}$ on a grid of candidate positions and pick the most likely position to initialize the BFGS algorithm that maximizes $\mathcal{L}_{\text{AoA/ToA}}^{(l)}$ over \mathbf{x} , with nuisance parameter τ_{TX} :

$$\left(\hat{\mathbf{x}}^{(l)}, \hat{\tau}_{\text{TX}}^{(l)}\right) = \arg \max_{(\mathbf{x}, \tau_{\text{TX}})} \mathcal{L}_{\text{AoA/ToA}}^{(l)}(\mathbf{x}, \tau_{\text{TX}})$$

3) *Results*: The colorized location estimates $\hat{\mathbf{x}}^{(l)}$ obtained through joint triangulation and multilateration are shown in Fig. 2c. The L-shape of the environment is preserved, but the overall quality of position estimates appears to be very similar to the purely triangulation-based method (Fig. 2b), with somewhat fewer outliers. A more detailed analysis of performance metrics in Section VI reveals that joint triangulation and multilateration slightly improves performance over just triangulation, as is to be expected.

IV. CHANNEL CHARTING-BASED LOCALIZATION

A. Dissimilarity Metric

We use an approach that we call *dissimilarity metric-based Channel Charting* and that we previously described in [4]. In the following, we use our *geodesic, fused* dissimilarity metric, which combines information extracted from the angle-delay profile (ADP) and from timestamp differences. Refer to [4] for information on how this metric is computed. We denote the dissimilarity between the datapoints l_x and l_y according to said metric by $d_{\text{G-fuse}}^{(l_x, l_y)}$.

B. Siamese Neural Network

We implement the forward charting function (FCF) $\mathcal{C}_\theta : \mathbb{C}^{B \times M_{\text{row}} \times M_{\text{col}} \times N_{\text{sub}}} \rightarrow \mathbb{R}^2$, which maps CSI tensors $\mathbf{H}^{(l)}$ to channel chart positions $\mathbf{x}^{(l)} = \mathcal{C}_\theta(\mathbf{H}^{(l)})$, as a neural network (NN). The NN is trained as a Siamese neural network, as in [10]. The Siamese loss function that we use is inspired by Sammon's loss [11] and is defined in terms of two datapoints

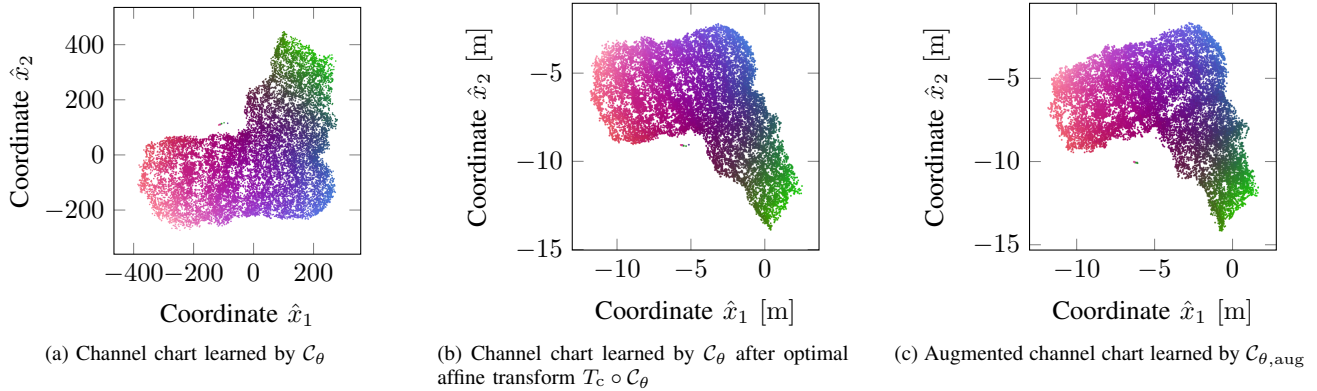


Fig. 3. Position estimates for Channel Charting-based source localization techniques

with indices l_x and l_y , whose channel chart coordinates are $\mathbf{x} = \mathcal{C}_\theta(\mathbf{H}^{(l_x)})$ and $\mathbf{y} = \mathcal{C}_\theta(\mathbf{H}^{(l_y)})$:

$$\mathcal{L}_{\text{siam}}^{(l_x, l_y)}(\mathbf{x}, \mathbf{y}) = \frac{\left(d_{\text{G-fuse}}^{(l_x, l_y)} - \|\mathbf{y} - \mathbf{x}\|_2\right)^2}{d_{\text{G-fuse}}^{(l_x, l_y)} + \beta} \quad (5)$$

$\mathcal{L}_{\text{siam}}^{(l_x, l_y)}$ describes an error measure between the Euclidean distance of predicted channel chart locations $\|\mathbf{y} - \mathbf{x}\|_2$ and the computed dissimilarity $d_{\text{G-fuse}}^{(l_x, l_y)}$. The parameter β is a hyperparameter that can tune Eq. (5) to weight either the absolute squared error (for large β) or the normalized squared error (for small β) higher. By evaluating the loss function over a batch of datapoint pairs (l_x, l_y) and backpropagation of gradients, the Siamese NN learns to map high-dimensional CSI to channel chart locations such that channel chart distances correspond best to the previously computed dissimilarities in the sense of Eq. (5).

C. Intermediate Results

By applying the learned forward charting function \mathcal{C}_θ to all channel tensors $\mathbf{H}^{(l)}$ in the dataset \mathcal{S} , we obtain the channel chart shown in Fig. 3a. While the channel chart preserves local datapoint neighborhood relationships and also reproduces the global L-shaped topology of the environment, it is arbitrarily scaled, rotated and flipped compared to the “ground truth” positions in Fig. 1c. This intuitively makes sense, since the FCF has no way of knowing anything about the absolute scale or orientation of the environment, as it is only trained on dissimilarities. Inspired by [3] and [12], we suggest to use the position estimates obtained through classical techniques (Section III) to estimate an affine transform T_c from the channel chart’s coordinate frame to physical coordinates.

D. Optimal Linear Transform

To find $T_c(\mathbf{x}) = \hat{\mathbf{A}}\mathbf{x} + \hat{\mathbf{b}}$, we solve the least squares problem

$$(\hat{\mathbf{A}}, \hat{\mathbf{b}}) = \arg \min_{(\mathbf{A}, \mathbf{b})} \sum_{l=1}^L \|\mathbf{A}\hat{\mathbf{x}}_{\text{CC}}^{(l)} + \mathbf{b} - \hat{\mathbf{x}}_{\text{AoA/ToA}}^{(l)}\|_2^2,$$

where $\hat{\mathbf{x}}_{\text{CC}}^{(l)} = \mathcal{C}_\theta(\mathbf{H}^{(l)})$ denotes the position estimate obtained through Channel Charting, and $\hat{\mathbf{x}}_{\text{AoA/ToA}}^{(l)}$ denotes the position

estimate obtained by ML optimization of $\mathcal{L}_{\text{AoA/ToA}}^{(l)}$. We write the composition of T_c and \mathcal{C}_θ , i.e., Channel Charting and subsequent application of T_c as $T_c \circ \mathcal{C}_\theta$.

E. Results

The channel chart after the optimal affine transform is shown in Fig. 3b. Clearly, the chart in Fig. 3b is identical to the one in Fig. 3a, except for the affine transform. The channel chart very much resembles the L-shaped map of “ground truth” positions, and orientation and scale now also match the reference.

As an aside, the learned FCFs \mathcal{C}_θ and $\mathcal{C}_{\theta, \text{aug}}$ were evaluated on \mathcal{S} , i.e., the same dataset that they were trained on. Since Channel Charting is a self-supervised learning technique, a test set is not strictly needed to get a meaningful performance evaluation. In some additional experiments, we also evaluated both \mathcal{C}_θ and $\mathcal{C}_{\theta, \text{aug}}$ on a test set of strictly different datapoints that was measured in the same environment and did not observe a significant drop in performance.

V. AUGMENTED CHANNEL CHARTING

In Section IV, Channel Charting and transforming channel chart coordinates into physical coordinates using classical position estimates were regarded as two separate steps. This has several disadvantages: For one, if there is a non-affine distortion in the channel chart coordinates, the affine transform T_c cannot correct for it, even if the distortion is not present in the classical position estimates. This effect is faintly visible in Fig. 3b: The angle between the two sides of the L-shape is too obtuse compared to the “ground truth” positions in 1c, even though the classical estimates in Fig. 2c clearly show a square angle. For another, the NN can easily take into account classical AoA and ToA estimates during training, without first reducing the information to position estimates. By factoring in similarity relationships, ToA estimates and also AoA estimates while training the FCF, all available information can be supplied to the NN at once. This is the idea behind what we will refer to as *augmented* Channel Charting, which we will explain in the following.

A. Dissimilarity Matrix Scaling

Before all sources of information (AoA / ToA / dissimilarities) can be taken into account in a unified framework, we first need to ensure compatibility. The dissimilarities $d_{G\text{-fuse}}^{(l_x, l_y)}$ are computed based on ADP and timestamps. While $d_{G\text{-fuse}}^{(l_x, l_y)}$ should ideally be proportional to the true Euclidean distance $\|\mathbf{x}^{(l_y)} - \mathbf{x}^{(l_x)}\|_2$ between datapoints l_x and l_y , there remains an unknown scaling factor γ , i.e., $d_{G\text{-fuse}}^{(l_x, l_y)} \approx \gamma \|\mathbf{x}^{(l_y)} - \mathbf{x}^{(l_x)}\|_2$. We estimate γ as

$$\hat{\gamma} = \frac{1}{L^2} \sum_{l_x=1}^L \sum_{l_y=1}^L \frac{d_{G\text{-fuse}}^{(l_x, l_y)}}{\|\hat{\mathbf{x}}_{\text{AoA/ToA}}^{(l_y)} - \hat{\mathbf{x}}_{\text{AoA/ToA}}^{(l_x)}\|_2}, \quad (6)$$

where $\hat{\mathbf{x}}_{\text{AoA/ToA}}^{(l)}$ is again the classical position estimate obtained by ML optimization of $\mathcal{L}_{\text{AoA/ToA}}^{(l)}$. Instead of estimating γ over all pairs of datapoints (l_x, l_y) , Eq. (6) may also be applied to a random subset of datapoint pairs to reduce computational complexity. We write the dissimilarities scaled by γ as

$$\tilde{d}_{G\text{-fuse}}^{(l_x, l_y)} = \frac{1}{\gamma} d_{G\text{-fuse}}^{(l_x, l_y)} \approx \|\mathbf{x}^{(l_y)} - \mathbf{x}^{(l_x)}\|_2.$$

B. Combined Loss Function

The key element of augmented Channel Charting is the *combined* loss function, which takes into account both a Siamese loss (similar to Eq. (5), but without normalization) and the classical AoA / TDoA-based likelihood function:

$$\mathcal{L}_{\text{comb}}^{(l_x, l_y)}(\mathbf{x}, \mathbf{y}) = (1 - \lambda) \left(\tilde{d}_{G\text{-fuse}}^{(l_x, l_y)} - \|\mathbf{y} - \mathbf{x}\|_2 \right)^2 - \lambda \left(\mathcal{L}_{\text{AoA/TDoA}}^{(l_y)}(\mathbf{y}) + \mathcal{L}_{\text{AoA/TDoA}}^{(l_x)}(\mathbf{x}) \right) \quad (7)$$

Note that minimizing $\mathcal{L}_{\text{comb}}^{(l_x, l_y)}$ simultaneously minimizes the Siamese loss given by the squared error term $(\tilde{d}_{G\text{-fuse}}^{(l_x, l_y)} - \|\mathbf{y} - \mathbf{x}\|_2)^2$ and maximizes the classical likelihood function $\mathcal{L}_{\text{AoA/TDoA}}^{(l)}$ for both datapoints l_x and l_y . The weighting of these two objectives is determined by the weighting factor λ , $0 \leq \lambda \leq 1$, which is a hyperparameter that may be adjusted over the training period. For example, λ may be assigned a high value in the beginning to quickly capture the global geometry, and lower values in subsequent NN training steps.

We want to point out that there is room for improvement for the combined loss function, in the sense that Eq. (7) mixes likelihood functions and a squared error term (which may be interpreted as a negative log-likelihood function). We chose to define the combined loss as given in Eq. (7) as it produced convincing results in our experiments.

C. Results

The channel chart learned with augmented Channel Charting is shown in Fig. 3c. It is similar to the one in Fig. 3b, but the edges of the shape are now straighter and there is a right angle between the two sides of the L-shape, just like in the “ground truth” map. Overall, the channel chart

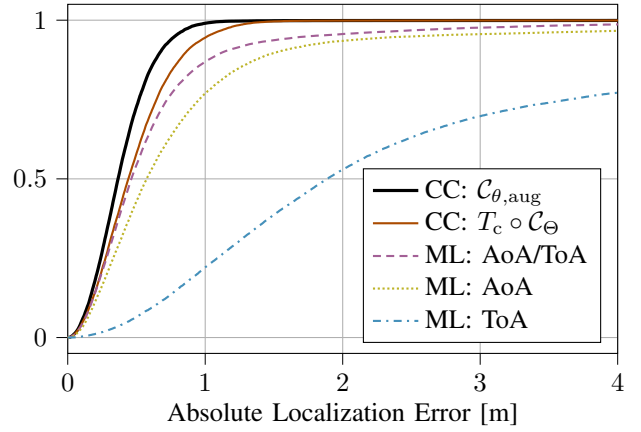


Fig. 4. Empirical cumulative distribution functions of absolute localization errors for all classical (maximum likelihood-based) and Channel Charting-based methods

looks very similar to the reference data. The performance metrics in Section VI show that augmented Channel Charting outperforms all the other source localization techniques.

VI. RESULTS, COMPARISON AND CONCLUSION

The top view maps for different localization techniques are shown in Fig. 2 and Fig. 3. Clearly, Fig. 3c approximates the “ground truth” positions in Fig. 1c best and also exhibits the smallest number of outlier estimates. To compare estimation techniques more objectively beyond this visual intuition, we introduce a set of formal performance criteria, which are commonly used in literature to quantify localization performance. We write the “ground truth” positions as $\mathbf{x}^{(l)}$ and the position estimates as $\hat{\mathbf{x}}^{(l)}$ and compute the metrics over the complete dataset \mathcal{S} . First of all, the mean absolute error (MAE) and distance root mean square (DRMS) are defined as

$$\text{MAE} = \frac{1}{L} \sum_{l=1}^L \|\mathbf{x}^{(l)} - \hat{\mathbf{x}}^{(l)}\|_2 \text{ and}$$

$$\text{DRMS} = \sqrt{\frac{1}{L} \sum_{l=1}^L \|\mathbf{x}^{(l)} - \hat{\mathbf{x}}^{(l)}\|_2^2}.$$

Furthermore, we define the circular error probable (CEP) and the 95th percentile radius (R95) as the median and 95th percentile of the empirical distribution of the localization error $\|\mathbf{x}^{(l)} - \hat{\mathbf{x}}^{(l)}\|_2$, and also consider the empirical cumulative distribution function (eCDF) of this error. Finally, we borrow the well-known dimensionality reduction performance metrics continuity (CT) and trustworthiness (TW) (level of preservation of local geometry), and Kruskal’s stress (KS) (level of preservation of global geometry) from Channel Charting literature, as defined, e.g., in [4] or [12]. We abbreviate the classical ML-based approach solely relying on ToA information (as in III-A) as “ML: ToA”, triangulation, which solely uses AoA information (as in III-B) as “ML: AoA” and the classical approach with the joint likelihood function (as in III-C) as

TABLE I
PERFORMANCE COMPARISON OF ALL CLASSICAL (MAXIMUM LIKELIHOOD-BASED) AND CHANNEL CHARTING-BASED METHODS

	Loss	MAE ↓	DRMS ↓	CEP ↓	R95 ↓	KS ↓	CT/TW ↑
ML: ToA	$\mathcal{L}_{\text{ToA}}^{(l)}$	2.314 m	3.090 m	1.715 m	6.298 m	0.980	0.871/0.933
ML: AoA	$\mathcal{L}_{\text{AoA}}^{(l)}$	0.909 m	1.643 m	0.574 m	2.563 m	0.236	0.932/0.936
ML: AoA / ToA	$\mathcal{L}_{\text{AoA/ToA}}^{(l)}$	0.676 m	1.228 m	0.462 m	1.763 m	0.214	0.965/0.970
CC: $T_c \circ C_\theta$	$\mathcal{L}_{\text{sjam}}^{(l)}$	0.490 m	0.584 m	0.441 m	1.026 m	0.071	0.996/0.996
CC: $C_{\theta,\text{aug}}$	$\mathcal{L}_{\text{aug}}^{(l)}$	0.401 m	0.483 m	0.369 m	0.789 m	0.070	0.995/0.995

“ML: AoA/ToA”. We abbreviate the Channel Charting-based solution that applies the optimal affine transform (as in IV-D) as “CC: $T_c \circ C_\theta$ ” and augmented Channel Charting as “CC: $C_{\theta,\text{aug}}$ ”.

The eCDFs in Fig. 4 show, unsurprisingly, that joint (AoA/ToA) classical ML optimization outperforms pure triangulation or multilateration. Pure AoA-based triangulation is much better than pure ToA-based multilateration, which is expected given the relatively low signal bandwidth and the small geometric scale of the measurement environment. Most importantly, though, the eCDFs in Fig. 4 also show that the two Channel Charting-based methods clearly outperform all classical techniques. The same conclusion can be arrived at by comparing the performance metrics in Tab. I: The two Channel Charting-based techniques outperform the classical methods with respect to all metrics. Augmented Channel Charting outperforms regular Channel Charting with subsequent affine transform with respect to all metrics except for CT and TW. However, the difference in CT / TW, and hence preservation of local geometry, is negligible compared to the significant localization performance gains of augmented Channel Charting over regular Channel Charting.

This leads us to the following conclusion: Not only can Channel Charting be enhanced by taking into account information from classical localization techniques, but Channel Charting can also be used to improve overall localization accuracy. One might argue that there exist better classical localization techniques than just the ones presented here (e.g., ones that also take into account received powers, elevation angles or phase differences of arrival between different arrays). If that is the case, the performance gap between Channel Charting and these classical techniques may shrink. However, with the framework of augmented Channel Charting, the additional information derived through classical techniques may be taken into account while training the FCF. With a suitable NN architecture, suitable features and sufficient training data, the universal approximation theorem should thus ensure that the learned FCF is always at least as good as the classical solution.

VII. OUTLOOK

We not only demonstrated that Channel Charting can outperform classical source localization techniques in terms of localization performance, but also showed that Channel Charting may be improved by taking into account information derived through classical AoA or ToA-based approaches. To this end, the augmented Channel Charting framework was put forward, which, in the future, may also take into account other

sources of side information available to the system. While we investigated Channel Charting as a source localization technique in this paper, we want to stress that the improvements in localization performance through augmented Channel Charting may also benefit other applications of Channel Charting, like handover prediction or pilot assignment.

REFERENCES

- [1] C. Studer, S. Medjkouh, E. Gönültaş, T. Goldstein, and O. Tirkkonen, “Channel Charting: Locating Users within the Radio Environment using Channel State Information,” *CoRR*, vol. abs/1807.05247, 2018.
- [2] S. Taner, V. Palhares, and C. Studer, “Channel Charting in Real-World Coordinates,” *arXiv preprint arXiv:2308.14498*, 2023.
- [3] J. Pihlajasalo, M. Koivisto, J. Talvitie, S. Ali-Löytty, and M. Valkama, “Absolute positioning with unsupervised multipoint channel charting for 5g networks,” in *2020 IEEE 92nd Vehicular Technology Conference (VTC2020-Fall)*. IEEE, 2020, pp. 1–5.
- [4] P. Stephan, F. Euchner, and S. ten Brink, “Angle-Delay Profile-Based and Timestamp-Aided Dissimilarity Metrics for Channel Charting,” *arXiv preprint arXiv:2308.09539*, 2023.
- [5] F. Euchner, M. Gauger, S. Dörner, and S. ten Brink, “A Distributed Massive MIMO Channel Sounder for “Big CSI Data”-driven Machine Learning,” in *WSA 2021; 25th International ITG Workshop on Smart Antennas*, 2021.
- [6] F. Euchner and M. Gauger, “CSI Dataset dichasus-cf0x: Distributed Antenna Setup in Industrial Environment, Day 1,” 2022. [Online]. Available: <https://doi.org/doi:10.18419/darus-2854>
- [7] X. Li and K. Pahlavan, “Super-resolution TOA estimation with diversity for indoor geolocation,” *IEEE transactions on wireless communications*, vol. 3, no. 1, pp. 224–234, 2004.
- [8] M. Wax and T. Kailath, “Detection of signals by information theoretic criteria,” *IEEE Transactions on acoustics, speech, and signal processing*, vol. 33, no. 2, pp. 387–392, 1985.
- [9] M. Henninger, T. E. Abrudan, S. Mandelli, M. Arnold, S. Saur, V.-M. Kolmonen, S. Klein, T. Schlitter, and S. Ten Brink, “Probabilistic 5G Indoor Positioning Proof of Concept with Outlier Rejection,” in *2022 Joint European Conference on Networks and Communications & 6G Summit (EuCNC/6G Summit)*. IEEE, 2022, pp. 249–254.
- [10] F. Euchner, C. Eun Lee, and P. Stephan. (2023) Dissimilarity Metric-Based Channel Charting. [Online]. Available: <https://dichasus.inue.uni-stuttgart.de/tutorials/tutorial/dissimilarity-metric-channelcharting/>
- [11] J. Sammon, “A Nonlinear Mapping for Data Structure Analysis,” *IEEE Transactions on Computers*, vol. C-18, no. 5, pp. 401–409, 1969.
- [12] M. Stahlke, G. Yammine, T. Feigl, B. M. Eskofier, and C. Mutschler, “Indoor Localization with Robust Global Channel Charting: A Time-Distance-Based Approach,” *IEEE Transactions on Machine Learning in Communications and Networking*, pp. 1–1, 2023.